

3-23-2020

Design and analysis of a novel long-distance double tendon-sheath transmission device for breast intervention robots under MRI field


Xiaohong Jia
Harbin University of Science and Technology

Yongde Zhang
Harbin University of Science and Technology

Jingang Jiang
Harbin University of Science and Technology

Haiyan Du
Harbin University of Science and Technology

Yan Yu
Follow this and additional works at: <https://jdc.jefferson.edu/radoncfp>

 Part of the [Oncology Commons](#), and the [Radiation Medicine Commons](#)


[Let us know how access to this document benefits you](#)

Recommended Citation

Jia, Xiaohong; Zhang, Yongde; Jiang, Jingang; Du, Haiyan; and Yu, Yan, "Design and analysis of a novel long-distance double tendon-sheath transmission device for breast intervention robots under MRI field" (2020). *Department of Radiation Oncology Faculty Papers*. Paper 133.
<https://jdc.jefferson.edu/radoncfp/133>

This Article is brought to you for free and open access by the Jefferson Digital Commons. The Jefferson Digital Commons is a service of Thomas Jefferson University's [Center for Teaching and Learning \(CTL\)](#). The Commons is a showcase for Jefferson books and journals, peer-reviewed scholarly publications, unique historical collections from the University archives, and teaching tools. The Jefferson Digital Commons allows researchers and interested readers anywhere in the world to learn about and keep up to date with Jefferson scholarship. This article has been accepted for inclusion in Department of Radiation Oncology Faculty Papers by an authorized administrator of the Jefferson Digital Commons. For more information, please contact: JeffersonDigitalCommons@jefferson.edu.

Design and analysis of a novel long-distance double tendon-sheath transmission device for breast intervention robots under MRI field

Advances in Mechanical Engineering
2020, Vol. 12(3) 1–17
© The Author(s) 2020
DOI: 10.1177/1687814020904565
journals.sagepub.com/home/ade


Xiaohong Jia¹, Yongde Zhang¹ , Jingang Jiang¹, Haiyan Du¹ and Yan Yu²

Abstract

Cancer represents a major threat to human health. Magnetic resonance imaging (MRI) provides superior performance to other imaging-based examination methods in the detection of tumors and offers distinct advantages in biopsy and seed implantation. However, because of the MRI environment, the material requirements for actuating devices for the medical robots used in MRI are incredibly demanding. This paper describes a novel double tendon-sheath transmission device for use in MRI applications. LeBus grooves are used in the original transmission wheels, thus enabling the system to realize long-distance and large-stroke transmission with improved accuracy. The friction model of the transmission system and the transmission characteristics model of the novel tendon-sheath structure are then established. To address the problem that tension sensors cannot be installed in large-stroke transmission systems, a three-point force measurement method is used to measure and set an appropriate preload in the novel tendon-sheath transmission system. Additionally, experiments are conducted to verify the accuracy of the theoretical model and multiple groups of tests are performed to explore the transmission characteristics. Finally, the novel tendon-sheath transmission system is compensated to improve its accuracy and the experimental results acquired after compensation show that the system satisfies the design requirements.

Keywords

Double tendon-sheath, large-stroke transmission model, LeBus grooves, breast intervention robot, MRI, transmission device, friction model

Date received: 11 July 2019; accepted: 13 January 2020

Handling Editor: James Baldwin

Introduction

According to the global cancer statistics for 2018,¹ there are currently an estimated 18.19 million new cancer cases and 9.6 million cancer deaths per year. Cancer is a serious threat to human health and affects people's lives in both developed and developing countries. Magnetic resonance imaging (MRI) is widely used when performing biopsies and therapeutic surgery because it offers highly accurate cancer detection,^{2,3} provides high-definition and high-resolution images, and does not subject patients to radiation. The medical robots used

in MRI are attracting increasing attention from the international medical community^{4–6} and from scientific

¹Intelligent Machine Institute, School of Mechanical and Power Engineering, Harbin University of Science and Technology, Harbin, China
²Sidney Kimmel Medical College, Thomas Jefferson University, Philadelphia, USA

Corresponding author:

Yongde Zhang, Intelligent Machine Institute, School of Mechanical and Power Engineering, Harbin University of Science and Technology, #52 Xuefu Road, Nan'gang District, Harbin, Heilongjiang 150080, China.
Email: zhangyd@hrbust.edu.cn



researchers in recent years because of advantages that include high efficiency and minimally invasive performance. However, MRI uses a strong magnetic field. There are thus strict requirements for the selection of suitable materials for these robots and their drive systems.⁷⁻⁹ In addition, there is an urgent need for a robot driving method that is suitable for use in the nuclear magnetic environment because such a method would allow robots to assist in operations without affecting the MRI results.

The tendon-sheath concept has been widely used in medical and other types of robots¹⁰⁻¹³ because of its high transmission precision, light weight, smooth transmission, flexibility, and small size. Kaneko et al.^{14,15} studied the transmission characteristics of a simple tendon-sheath model for finger joint control. They reported an elastic hysteresis phenomenon in the transmission process and observed a change in the transmission stiffness when the transmission direction changed. Their model was limited to a constant transmission angle and constant preload, and the torque model and the hysteresis characteristics of the transmission device were verified from both experimental and simulation perspectives. Palli et al.¹⁶ proposed both static and dynamic models of tendon-sheath actuation systems. They also introduced a new viscoelastic model in which polymeric fibers were used as tendon materials for a robotic hand. A simple control strategy was proposed to compensate for nonlinear effects and a complex LuGre-like dynamic friction model was used to improve the controller reliability. Agrawal et al.^{17,18} proposed a set of continuous time-domain partial differential equations for a tendon-sheath structure with an arbitrary curvature and initial tension distribution. They also considered the effects of the MRI environment and time-varying nonlinear viscoelastic behavior. Their model can effectively analyze the backlash from motion, the relaxation phenomenon of the system, and the transmission tension between the two cables.

Phee et al.¹⁹⁻²¹ studied control of the precise positioning and the force feedback from robotic arms used in natural orifice transluminal endoscopic surgery. Nonlinear adaptive control algorithms and real-time enhancements for tracking were designed to improve the performance of the cable-conduit mechanisms. They also developed a motion control device, a telesurgical workstation and a slave manipulator. Schiele et al.^{22,23} investigated a new type of tendon-sheath actuator to perform force-reflection to a wearable exoskeleton. They proposed a hardware prototype in which springs ensured the constant preloading associated with the packaging angles. The transmission characteristics of the tendon-sheath system between the actuator and the robot joint were also analyzed.

Jiang et al.^{24,25} designed and analyzed MRI-compatible surgical robots for breast puncture and prostate

needle insertion operations. In their approach, the tendon-sheath systems were used for power transmission over comparatively long distances. Wang et al.^{26,27} established a transmission model for a double tendon-sheath structure under arbitrary load conditions and analyzed many non-ideal and nonlinear tendon-sheath transmission problems. They also built an experimental tendon-sheath platform and applied friction and control compensation measures to the tendon-sheath transmission.

Currently, the joints of the manipulators of medical robots, and particularly surgical robots, are often driven using tendon-sheath systems. The transmission wheels of these tendon-sheath systems are usually made from metal and are primarily designed for single-slot and single-layer arrangements. The range of possible transmission angles is typically small. However, MRI-compatible interventional surgical robots require a transmission system that can be driven over a wide range of angles and over long distances within a limited space. In addition, the commonly used transmission wheels with thread grooves often suffer from the phenomena of empty ropes and stacked ropes when the wheels are winding; in the former case, the tendon is wound in multiple grooves for a single lap, while in the latter case, the tendon is wound for multiple laps in one groove. Regardless of whether these phenomena occur in the first layer or in multiple layers, this will affect the winding accuracy.

Based on previous studies, this paper describes a new type of tendon-sheath transmission device that combines long-distance power transmission with nuclear magnetic compatibility. LeBus grooves are used in the transmission wheels to solve the problem of random winding during tendon-sheath multi-layer transmission; this allows the transmission accuracy to be further improved. The motor can be located away from the MRI source to avoid affecting the imaging, and power can be transmitted to the robot on the nuclear magnetic resonance apparatus via the tendon-sheath system. In this way, the problem of nuclear magnetic incompatibility can be solved and the service life of the tendon-sheath device can be extended.

Design and friction study of double tendon-sheath transmission wheels with LeBus grooves

The proposed tendon-sheath system uses nonmetallic materials to meet the requirements of the nuclear magnetic environment. Figure 1 illustrates use of the proposed system in a nuclear magnetic environment. Long-distance and wide-range transmission can be realized and the sizes of the transmission wheels are minimized to satisfy force demands (including space constraints).

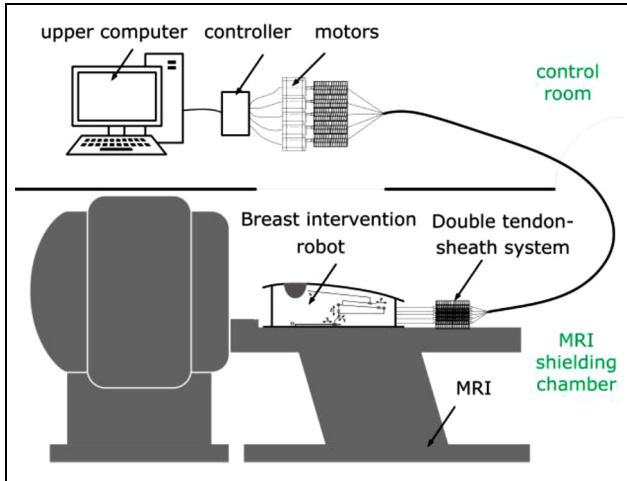


Figure 1. Application of a new type of tendon-sheath transmission device in an MRI environment.

Therefore, the transmission wheels arrangement will use a multi-layer winding method. However, there will inevitably be contact between the upper and lower layers of the tendon or between adjacent tendons that are wound within the same layer. Friction between adjacent tendons caused by extrusion means that the contact point of the tendon is subjected to a sliding friction force during movement. Therefore, the stress characteristics of the novel tendon-sheath transmission system must be analyzed.

The tendon used in the proposed system is composed of eight slender, flexible strands. Because a single flexible tendon is relatively small in size, it is necessary to determine the areas where damage to the device could occur and to characterize the fatigue wear of the tendon. However, changes in the infinitesimal displacement relative to the size of the overall flexible tendon

are of low significance. Therefore, to simplify the calculations and obtain analytical data about the macroscopic stresses, the tendon is considered as a cylinder here. The transmission winding mode of the double tendon-sheath is illustrated in Figure 2. The driving wheel uses left-hand threads while the follower wheel uses right-hand threads, so the transmission directions of the wheels remain consistent. In the initial state, the thread grooves on side B of the driving wheel and the thread grooves on side A of the follower wheel are wound all over the wheel and these windings cover the same n layers (where n is a positive integer). The thread grooves on side A of the driving wheel and those on side B of the follower wheel are then unwound. Arrows indicate the rotation of the transmission wheels, and the two transmission wheels are oriented parallel to one another.

During the winding process, the axis of the tendon changes from the fleet angle (i.e., the angle between the center line of the tendon and the plane perpendicular to the axis of the transmission wheel) to the helical angle of the transmission wheel. To enable calculation of the variations in the bending angle and the friction force of the tendon during the process of multi-layer winding of a double broken-line transmission wheel, the angle that represents the transformation of the tendon from the fleet angle γ to the helical angle ϕ is defined as the deflection angle β . As shown in Figure 2, where the direction is indicated by an arrow, the positive direction runs clockwise. For convenience of calculation, we only consider the friction generated by the regular contact parts of the tendon during the multi-layer winding process and ignore the friction that occurs during the transitions between the different layers.

To indicate the frictional force of the multi-layer winding of the tendon, the LeBus grooves on the right-

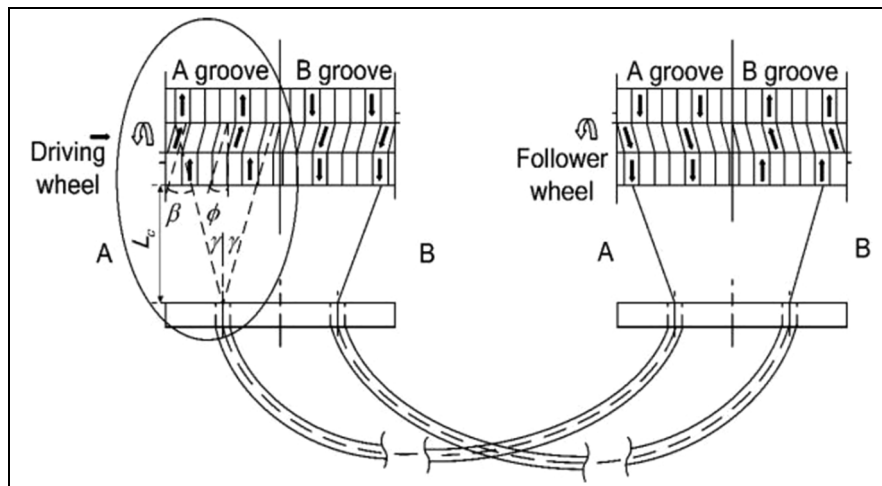


Figure 2. Schematic diagram of double tendon-sheath and helical angle distribution of the transmission winding mode.

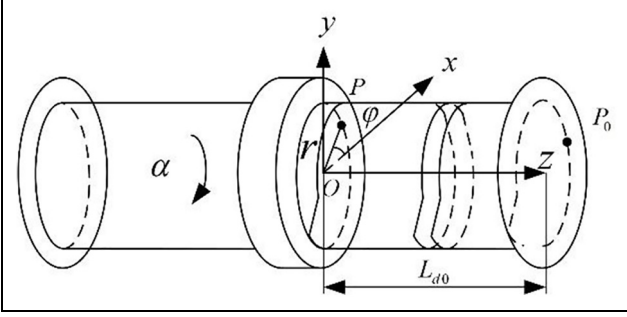


Figure 3. Schematic diagram showing the spatial rectangular coordinate system and the cylindrical coordinate system in the transmission wheel.

hand side of the driving wheel are used as an example. As shown in Figure 3, the spatial rectangular coordinate system of the transmission wheel denoted by $O-XYZ$ is established in a relatively static state. The origin O of the coordinate system is located at the center of the transmission wheel. The XOY plane lies perpendicular to the axis of the driving wheel. The right-hand side of the driving wheel indicates the positive direction of the z -axis.

To describe the position and calculate the friction force of the tendon on the transmission wheels, a corresponding cylindrical coordinate system is established based on the rectangular $O-XYZ$ coordinates of the transmission wheel. X , Y , and Z represent the coordinate values of the points on the tendon in the spatial rectangular coordinate system and (r, φ, z_p) represent the coordinate values of the points on the tendon in the cylindrical coordinate system. Any point p in the first layer of the tendon in the transmission wheel is denoted in cylindrical coordinates by (r, φ, z_p) . The relationship between the spatial rectangular coordinate system and the cylindrical coordinate system at any point in the transmission wheel is given as follows:

$$z_p = \begin{cases} L_{d0} - nP_s \\ L_{d0} - nP_s - \frac{P_s}{2\alpha_b}(\alpha - 360^\circ \cdot n - \alpha_s) \\ L_{d0} - \frac{P_s}{2}(2n + 1) \\ L_{d0} - \frac{P_s}{2}(2n + 1) - \frac{P_s}{2\alpha_b}(\alpha - 360^\circ \cdot n - 180^\circ - \alpha_s) \end{cases} \quad \begin{cases} x = r \cos \varphi \\ y = r \sin \varphi \\ z = z_p \end{cases} \quad (1)$$

The starting point of the tendon winding on the driving wheel is P_0 , which is located in the XOZ plane

on the right-hand side of the driving wheel. The tendon is wound in a left-hand manner. Ideally, when the driving wheel rotates by an angle α in the direction of the arrow around the center axis, the tendon is wound by the same angle around the LeBus grooves in the direction opposite to the rotation of the driving wheel. The width of the driving wheel required to accommodate the tendon is L_{d0} and the centerline of the tendon winding is, by default, oriented along the centerline of the driving wheel. Because the diameter of the tendon is much smaller than that of the driving wheel, the driving wheel diameter can be regarded as the diameter of the tendon winding on the driving wheel, denoted by D . The angle θ indicates the rotation of the tendon on the driving wheel, i.e., the angle of rotation relative to the initial point. For the case of LeBus grooves, the trajectory curve of tendon winding on the transmission wheel can be expressed in the cylindrical coordinate system as:

$$\begin{cases} r = r_{p0} \\ \varphi = -\theta \end{cases} \quad (2)$$

Figure 3 shows that when the transmission wheel rotates by 360° , it will experience two straight grooves and double broken-line grooves, where the combined rotation angle of a straight groove and a broken-line groove is 180° . Let the lengths of the straight grooves and the broken-line grooves of the transmission wheel when rotating by 360° in the direction perpendicular to the axis of the driving wheel be l_s and l_b , respectively. The angle at which the tendon winds around each straight groove is α_s , and the angle at which the tendon winds around each broken groove is α_b .

These two angles can be expressed as:

$$\begin{cases} \alpha_s = \frac{90}{\pi r} l_s \\ \alpha_b = \frac{90}{\pi r} l_b \end{cases} \quad (3)$$

Therefore, z_p can be expressed as follows:

$$\begin{aligned} 2n \bullet 180^\circ < \alpha < 2n \bullet 180^\circ + \alpha_s \\ 2n \bullet 180^\circ + \alpha_s < \alpha < 2(n + 1) \bullet 180^\circ \\ 2(n + 1) \bullet 180^\circ < \alpha < 2(n + 1) \bullet 180^\circ + \alpha_s \\ 2(n + 1) \bullet 180^\circ + \alpha_s < \alpha < 2(n + 2) \bullet 180^\circ \end{aligned} \quad (4)$$

where P_s is the pitch of one rotation of the transmission wheel, $P_s = l_b \tan \phi$, and $n = 0, 1, 2, \dots$ is the number of cycles in which the tendon is wound onto the driving wheel.

As Figure 2 shows, the distance between the baffle on which the sheath is placed and the tendon on the driving wheel is L_c .

Assuming that the tendon is in an ideal condition in terms of its winding and tightening on the driving wheel, when the tendon is located within the $\frac{L_{d0}}{2} - L_{d0}$ range on either side of the transmission wheel, the fleet angle is given by:

$$\gamma_f = \arctan \frac{Z_p - \frac{L_{d0}}{2}}{L_c} \quad (5)$$

When the tendon is located in the range from $0 - \frac{L_{d0}}{2}$ on either side of the transmission wheel, the fleet angle is given by:

$$\gamma_n = \arctan \frac{\frac{L_{d0}}{2} - Z_p}{L_c} \quad (6)$$

The friction force of the tendon on the transmission wheel is related to both the fleet angle γ and the helical angle ϕ of the system, the diameter of the transmission wheel, and the structure and the mechanical properties of the tendon itself. The winding force of the tendon is much more complex in the transitional stage, and the stroke is shorter, which means that it has less of an influence on the friction force of the tendon in the overall transmission process. Therefore, the analysis of the friction force of the broken-line segment must also consider the situation where a straight segment is wound around the transmission wheel. The tension of the tendon is F_c , the sliding friction factor between the tendons is μ , and the circumferential winding force produced by the tendon winding around the transmission wheel is F_q . The circumferential winding force F_{q1} generated by the winding of the tendon in the first layer can be expressed as:

$$F_{q1} = 2F_c \cos \gamma / D \quad (7)$$

and the friction force of the first layer of the transmission wheel F_{f1} can be expressed as:

$$F_{f1} = \mu F_{q1} \quad (8)$$

Therefore, the friction force F_{f1} can be expressed as:

$$F_{f1} = 2\mu F_c \cos \gamma / D \quad (9)$$

As shown in Figure 4, in most areas, the second layer of the tendon is wound systematically in the grooves arranged in the first layer of the tendon and this can be considered to be a triangular arrangement. This arrangement is relatively stable and thus the second layer of the tendon can be regarded as being supported by the bottom layer only. The same is true for multi-layer windings of the tendon and there is no trend for mutual movement. At this point, the stress of the tendon can be expressed as follows:

$$F_{f2} = 2\mu N_p \quad (10)$$

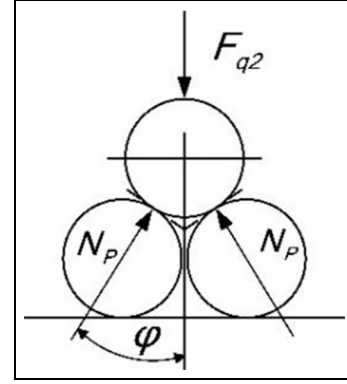


Figure 4. Schematic diagram of stress of the second layer of the tendon on the transmission wheel.

where N_p is the extrusion force between the two layers of the tendons and is given by:

$$N_p = F_{q2} / 2 \cos \phi \quad (11)$$

and ϕ represents the angle between the winding force of the transmission wheel and the direction normal to the contact surface of the tendon. The geometric relationship between the upper and lower layers of the tendon can be approximated as an equilateral triangle and thus $\phi \approx 30^\circ$. The circumferential winding force F_{q2} generated by the winding of the tendon in the second layer can be expressed as:

$$F_{q2} = 2F_c \cos \gamma / D_2 \quad (12)$$

Because the diameter of the tendon is very small relative to the diameter of the transmission wheel, D_2 can be approximated as D . From equations (10)–(12), we then obtain:

$$F_{f2} = 4\sqrt{3}\mu F_c \cos \gamma / 3D \quad (13)$$

Because the winding of the tendon during transmission is mostly in triangular form, the friction force of the tendon in layer $N^* + 2$ (where N^* is a positive integer) can be calculated using equation (13) in the case of winding of multiple layers. It is only necessary to consider the transmission wheel diameter after winding of the tendon based on the diameter of the actual transmission wheel and the diameter of the tendon.

Research on nonlinear transmission characteristics of the double tendon-sheath with LeBus grooves

Unit and unidirectional motion formulas

In the transmission process of the double tendon-sheath system, the elastic elongation deformation of a tendon

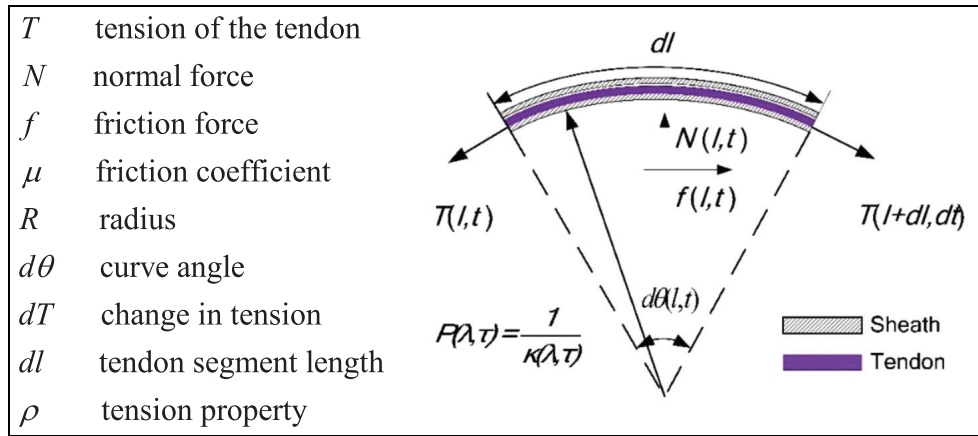


Figure 5. Force balance of a tiny segment of the tendon-sheath system.

with no relative motion on the transmission wheel is not taken into account—only the friction between the transmission wheel and the tendon, the friction between the tendon and the sheath, and the elastic elongation deformation of the tendon are considered. The force of the small static element in the double tendon-sheath system is analyzed first. In Figure 5, the following notation is used.

The force model of the tendon is shown in Figure 5 and the relational formulas are as follows:

$$\begin{cases} d\theta(l, t) = dl/R(l, t) \\ N(l, t) = T(l, t)d\theta(l, t) \\ f(l, t) = dT(l, t) = \mu N(l, t) \end{cases} \quad (14)$$

where T is the tension of the tendon, N is the normal force, f is the friction force, μ is the friction coefficient, R is the radius, $d\theta$ is the curve angle, dT is the change in tension, and dl is the tendon segment length.

If the coefficient of dynamic friction is equal to the coefficient of static friction, then the following equation can be obtained:

$$\frac{d\theta(l, t)}{T(l, t)} = \mu \frac{dl}{R(l, t)} \quad (15)$$

Let $T_0(l, t)$ be the initial value of the tension of the flexible cable before transmission and l be the total arc length of the distance transmitted by the system. The above equation is based on the assumption that the sheath has only one overall bending radius, R . However, in practice, the bending radius and the number of bends of the tendon and the sheath could both be arbitrary, as shown in Figure 6.

Therefore, the tendon of the i th segment can be represented by:

$$T_i(l, t) = T_0(0, t)e^{(-\mu \frac{l_1}{R_1(l, t)} - \mu \frac{l_2 - l_1}{R_2(l, t)} - \dots - \mu \frac{l_n - l_{n-1}}{R_n(l, t)}) \text{sign}(\xi)} \quad (16)$$

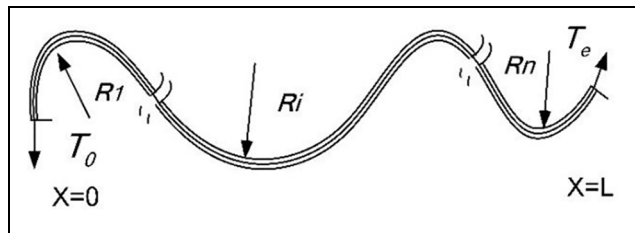


Figure 6. Schematic diagram of tendon-sheath transmission with arbitrary curvature.

where $\text{sign}(\xi)$ is the direction function and ξ is the tendon displacement at the driving wheel, such that:

$$\text{sign}(\xi) = \begin{cases} 1 & (\xi > 0) \text{ pull phase} \\ -1 & (\xi < 0) \text{ release phase} \end{cases}$$

For a tendon-sheath system with an arbitrary bending radius (even in the case of a straight line), the tension at any point can be calculated using equation (16), which represents an improved Euler equation for friction transmission in the tendon-sheath structure. Using this equation, the elastic deformation of the tendon caused by changes in tension under the action of an external load can be calculated.

Let l_i be the length of the tendon from the starting point of the transmission to the end point of the i th segment of an arc. The tension at the end of the tendon is then given by:

$$T_e(l, t) = T_0(0, t)e^{(-\mu \frac{l_1}{R_1(l, t)} - \mu \frac{l_2 - l_1}{R_2(l, t)} - \dots - \mu \frac{l_n - l_{n-1}}{R_n(l, t)}) \text{sign}(\xi)} \quad (17)$$

Let the intermediate variable λ be expressed as:

$$\lambda = \mu \frac{l_1}{R_1(l, t)} + \mu \frac{l_2 - l_1}{R_2(l, t)} + \dots + \mu \frac{l_n - l_{n-1}}{R_n(l, t)} \quad (18)$$

The relationship of the parameters l and R to the force output in the transmission part can then be obtained via the intermediate parameter λ by analyzing the tendon in its various states of motion:

$$T_e(l, t) = T_0(l, t)e^{-\lambda \text{sign}(\xi)} \quad (19)$$

If we consider the elastic deformation of the tendon-sheath transmission device studied in this paper, the elongation of the tendon can be expressed as:

$$\Delta L = \frac{T}{EA}L \quad (20)$$

i.e.,

$$\Delta L = \int_0^l \frac{T(l, t)}{EA} dl = \frac{T(0, t)}{EA} \int_0^l e^{-\lambda \text{sign}(\xi)} dl \quad (21)$$

where the speed of movement of the tendon is ξ , the tendon elongation is ΔL , the elastic modulus of the tendon is E , the Coulomb friction coefficient is τ , and the cross-sectional area of the tendon is A .

Bidirectionally coupled motion model of the tendon-sheath structure

The bidirectionally coupled transmission model of a double tendon-sheath structure with nonlinear characteristics that can realize long-distance and large-stroke driving not only differs from the long-distance single tendon-sheath transmission model, but also differs from the long-distance, small-stroke double tendon-sheath transmission model. The proposed system must combine the transmission characteristics of the single tendon-sheath structure with the bidirectionally coupled characteristics of the double tendon-sheath structure to solve the hysteresis, transmission backlash, and direction-dependence phenomena that often occur during the transmission process. To solve these problems, it is essential to establish a reasonable mathematical model of the structure from which an efficient and stable solution can be derived.

The bidirectional coupled transmission of a double tendon-sheath structure that can realize long-distance and large-stroke driving requires continuous multi-turn rotation of the transmission wheels during movement. At the same time, the deformation should be generated by the movement of the tendon in the sheath. Therefore, the system return error is mainly composed of the nonlinear distortion of the tendon during the transmission process and the friction of the transmission wheels when they are affected by the load. Figure 7 shows a schematic diagram of the coupled motion model of the tendon-sheath system when driven using a motor.

Figure 7 shows that the two ends of tendon a and tendon b are fixed at the driving wheel and the follower

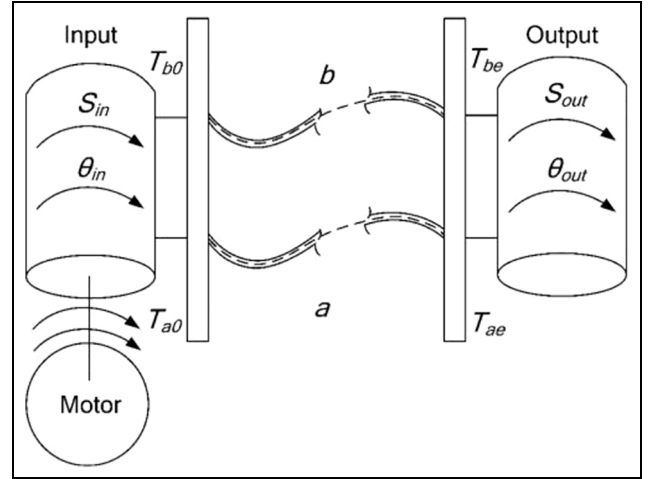


Figure 7. Schematic diagram of double tendon-sheath transmission model.

wheel, respectively. The input angle of the driving wheel is θ_{in} and the output angle of the follower wheel is θ_{out} . S_{in} is the tendon rotation length in the driving wheel and S_{out} is the tendon rotation length in the follower wheel. Both tendons follow a similar transmission line. By default, the changes in the curvatures of the two tendons along the length direction are the same.

Let the direction of movement of tendon a denote the positive direction of the movement and let tendon b move in the negative direction when the driving wheel rotates clockwise. When the tendon moves in the positive direction, the sliding direction exponent is defined as 1; when the tendon moves in the opposite direction, the sliding direction exponent is then -1 . When the system driving wheel is driven clockwise, the output relationship of the force is described as follows, based on equation (19):

$$\begin{aligned} T_{ae}(l, t) &= T_{a0}(0, t)^{-\lambda \text{sign}(\xi)} & \xi > 0 \\ T_{be}(l, t) &= T_{b0}(0, t)^{-\lambda \text{sign}(\xi)} & \xi < 0 \end{aligned} \quad (22)$$

where $T_{ao}(l, t)$ and $T_{ae}(l, t)$ are the tensile values at the beginning and the end of tendon a , respectively. Similarly, $T_{bo}(l, t)$ and $T_{be}(l, t)$ are the tensile values at the beginning and the end of tendon b , respectively.

The tension of the tendon when winding around the transmission wheel in a static condition is defined as $T_0(0, t)$. The deformations of the tendons can be obtained from the elastic deformation formula for a tendon during transmission, as follows:

$$\begin{aligned} \Delta L_a^+ &= \frac{T_{ao}(l, t) - T_0(0, t)}{EA} \int_0^l e^{-\lambda \text{sign}(\xi)} dl \\ \Delta L_b^+ &= \frac{T_{be}(l, t) - T_0(0, t)}{EA} \int_0^l e^{-\lambda \text{sign}(\xi)} dl \end{aligned} \quad (23)$$

However, during the transmission process, the driving wheel must also overcome the friction of the tendon from the transmission wheels. The two-layer tendon winding in the transmission wheel is used as an example and the theory for multi-layer tendons is similar.

Let S_{ain} and S_{bin} be the rotation lengths of tendons a and b in the driving wheel, respectively. Let S_{aout} and S_{bout} be the rotation lengths of tendons a and b in the follower wheel, respectively. The actual deformation of the two tendons during motion is then given by:

$$\begin{aligned}\Delta L_{aw}^+ &= \frac{T_{ao}(l, t) - T_0(0, t) - F_{f2}}{EA} \int_0^l e^{-\lambda \text{sign}(\xi)} dl \\ \Delta L_{bw}^+ &= \frac{T_{bo}(l, t) - T_0(0, t) + F_{f2}}{EA} \int_0^l e^{-\lambda \text{sign}(\xi)} dl\end{aligned}\quad (24)$$

Therefore, the actual displacements of the driving wheel for the two tendons are:

$$\begin{aligned}S_{ain}(l, t) &= \Delta L_{aw}^+ + S_{aout}(l, t) \\ S_{bin}(l, t) &= \Delta L_{bw}^+ + S_{bin}(l, t)\end{aligned}\quad (25)$$

On the output side, the displacements of tendon a and tendon b should be equal, i.e.,

$$S_{aout}(l, t) = S_{bout}(l, t) \quad (26)$$

By substituting equation (26) into equation (25), the displacement difference of the two tendons at the input side during clockwise driving is given by:

$$\Delta S^+(l, t) = S_{ain}(l, t) - S_{bin}(l, t) = \Delta L_{aw}^+ + \Delta L_{bw}^+ \quad (27)$$

Therefore, when the direction of motion changes, the hysteresis angle can be determined. The formula for the backlash-like hysteresis angle is:

$$\theta_b(l, t) = \Delta S^+(l, t)/r \quad (28)$$

The angles of the driving wheel and the follower wheel can thus be obtained as:

$$\begin{aligned}\theta_{in}^+(l, t) &= S_{ain}(l, t)/r \\ \theta_{out}^+(l, t) &= S_{bout}(l, t)/r\end{aligned}\quad (29)$$

Based on the formulas above, the relational expression for the output angle is:

$$\theta_{out}^+(l, t) = \frac{S_{ain}(l, t) - \Delta L_{aw}^+}{r} \quad (30)$$

After multiple experiments, it was demonstrated that at the initial moment, when the transmission wheel rotates in one direction, the tendon moving in the opposite direction on the other side will always produce a relaxation phenomenon; this occurs even if the two

tendons are in tension and regardless of the magnitude of the pre-stress. This phenomenon will continue until a change in direction occurs, and when the transmission wheel has overcome the displacement difference of the tendons and the loose tendon begins to gradually tighten. The movement of the tendon will then continue to pass. This phenomenon can be proved and verified experimentally.

Similarly, when the driving wheel needs to change direction after positive movement, the output relationship of the force is:

$$\begin{aligned}T_{ae}(l, t) &= T_{a0}(0, t)^{-\lambda \text{sign}(\xi)} \quad \xi < 0 \\ T_{be}(l, t) &= T_{b0}(0, t)^{-\lambda \text{sign}(\xi)} \quad \xi > 0\end{aligned}\quad (31)$$

If the winding range of the tendon in the driving wheel does not reach the second layer after the positive movement, the friction will be F_{f1} . If the winding range of the tendon in the driving wheel does reach the second layer after the positive movement has ended, then the actual deformation of the tendon in motion is:

$$\begin{aligned}\Delta L_{aw}^- &= \frac{T_{ae}(l, t) - T_{a0}(0, t) + F_{f2}}{EA} \int_0^l e^{-\lambda \text{sign}(\xi)} dl \\ \Delta L_{bw}^- &= \frac{T_{b0}(l, t) - T_{be}(0, t) - F_{f2}}{EA} \int_0^l e^{-\lambda \text{sign}(\xi)} dl\end{aligned}\quad (32)$$

However, before the driving end of tendon b can drive the follower end of tendon b , the driving wheel must rotate by the displacement difference caused by the positive movement.

Therefore, the actual displacement of the driving end of the two tendons is given by:

$$\begin{aligned}S_{aout}(l, t) &= \Delta L_{aw}^- + S_{ain}(l, t) \\ S_{bin}(l, t) &= \Delta S^+(l, t) + \Delta L_{bw}^- + S_{bout}(l, t)\end{aligned}\quad (33)$$

Consequently, the displacement difference between the two tendons after the reverse motion can be determined as follows:

$$\begin{aligned}\Delta S^-(l, t) &= S_{bin}(l, t) - S_{ain}(l, t) \\ &= \Delta L_{aw}^- + \Delta L_{bw}^- + \Delta S^+(l, t)\end{aligned}\quad (34)$$

Subsequently, the angular displacements of the driving wheel and the follower wheel when driving counter-clockwise can be calculated as:

$$\begin{aligned}\theta_{in}^-(l, t) &= S_{bin}(l, t)/r \\ \theta_{out}^-(l, t) &= S_{aout}(l, t)/r\end{aligned}\quad (35)$$

Based on the equations above, the relational expression for the output angle after the reverse motion is given by:

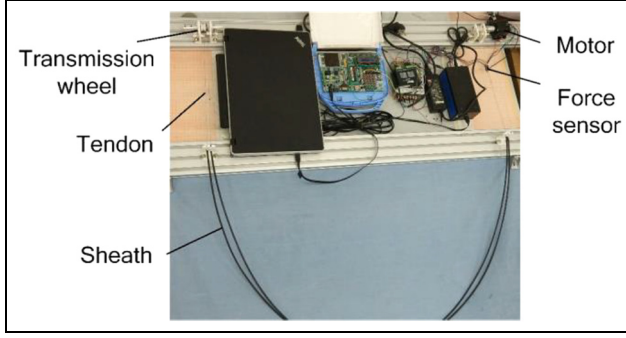


Figure 8. Experimental platform for tendon-sheath pre-tension transmission.

$$\theta_{\text{out}}^-(l, t) = \frac{S_{\text{bin}}(l, t) - \Delta L_{\text{aw}}^- - \Delta S^+(l, t)}{r} \quad (36)$$

The transfer process of the double tendon-sheath system can be analyzed using these equations. First, in the delay stage, after the direction of the driving wheel changes, the follower wheel displacement is invariant, with one of the tendons in a gradual tension state and the other tendon in a gradual relaxation state. The tendon inside the sheath is in partial motion and does not reach the follower wheel. Second, during the running stage, the two tendons are in motion simultaneously, but the tension on one side of the driving end is increasing while the tension on the other side of the tendon is decreasing. Finally, during the transition stage between the delay stage and the running stage, one tendon is in a state of tension and the other is in a state of partial motion, which indicates loosening from one side and gradual tightening from the other side. The motion of the double-tendon-sheath coupling is initially in the transition stage before entering the full running stage up to a predetermined position, and it then enters the delay stage when the direction is about to change.

From the equations above, the nonlinear characteristics of the hysteresis, the backlash-like hysteresis, and the directional dependence can be determined, and the friction coefficient of the tendon contact surface, the full curvature of the double tendon-sheath structure, and the equivalent elasticity of the tendon can also be calculated. The friction coefficient is related to the curve torsion rate, the transmission speed, and other factors. Research into the transmission characteristics of the double tendon-sheath system has important guiding significance for precise control of nonmetallic tendon-driven robots that require long-distance and large-stroke motion capabilities.

Determination of pre-tightening force parameters and their application

In accordance with the MRI operating requirements, the tendon in the proposed system is constructed using

a high-molecular-weight polyethylene fiber. This fiber has properties that include high strength, a high modulus, low fiber density, low elongation on breaking, high breaking resistance, and a strong energy absorption capability. Overall, this material offers outstanding impact resistance, shearing resistance, chemical resistance, and abrasion resistance, and also offers a long flexural life. If the preloading is too small, some slack will be present in the transmission process; however, if the preload is too high, the service life of the tendon and the transition phenomenon in transmission will be affected. Because the tendon is a nonmetallic wire elastic material, selection of a reasonable preload could effectively avoid the problems noted above. The experimental platform for the tendon-sheath system was constructed as shown in Figure 8 to aid in selection of the appropriate preload.

The experimental principle is described as follows. The two ends of the tension sensor were tied directly to the tendon. In a natural tension state, the preload on the tendon was 0 N. This preload could be increased by varying the position of the pulley on the slide of the tendon tensioning mechanism and the pulley position was changed in 3 mm steps with a maximum movement of 12 mm. When the tensioning mechanism pulley was moved along the slider by 3, 6, 9, and 12 mm, the corresponding pre-tension forces on the tendon were 0.6 N, 1.1 N, 1.7 N, and 1.9 N, respectively. Finally, the displacement difference between the input and output ends of the tendon was tested under different preloads. The experimental results are presented in Figure 9.

The experimental data show that the displacement differences between the input and output ends corresponding to unidirectional motion are approximately 2.8 ± 1.5 mm, 2.2 ± 1.0 mm, 1.7 ± 1.1 mm, 4.2 ± 1.1 mm, and 5.1 ± 2.2 mm under pre-tension forces of 0 N, 0.6 N, 1.1 N, 1.7 N, and 1.9 N, respectively. As shown in Figure 10, the Akima spline interpolation method was used to connect these curves. It is evident that the displacement difference between the input and output ends of the tendon was minimized when the preload on the tendon was 1.1 N in unidirectional motion. Therefore, under the experimental conditions, a value of approximately 1.1 N for the pre-tension force of the tendon is suitable.

In much of the literature, tendon-sheath transmission refers to a short-range and small-angle motion that can be used to measure the initial force directly using a tension sensor. Unlike most of these studies, however, the tendon-sheath system proposed here is designed to impart a driving force that can be transmitted over an extensive range. As a result, the tension of the tendon cannot be measured directly using a tension sensor. In the previous methods, it was also impossible to adjust the preload. Therefore, the three-point method was

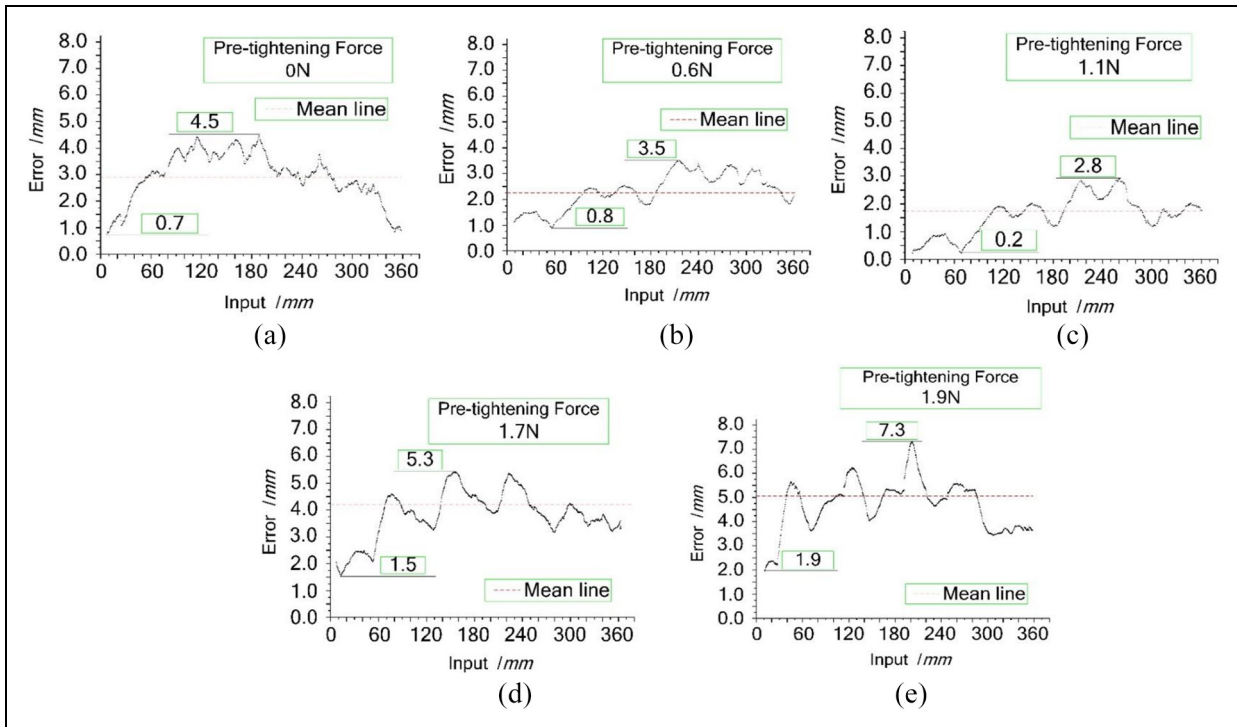


Figure 9. Input–output errors under different preload conditions.

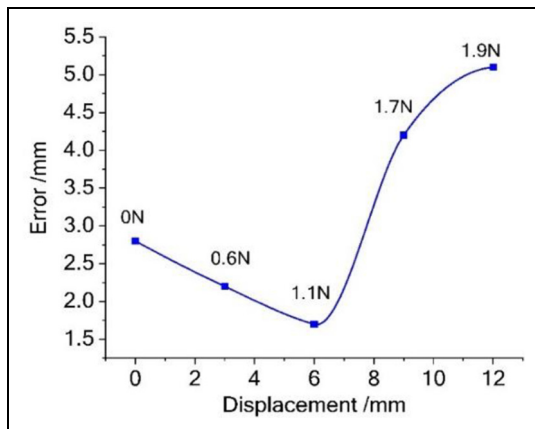


Figure 10. Variations in the mean errors for five preloads.

used to measure the initial strength indirectly by measuring the pressure at both ends of the tendon.

As shown in Figure 11, the preload force was measured using a six-dimensional force sensor based on a three-point measurement method for the preload on a small-diameter tendon. The distance between the two fixed bars was set at 70 mm. One end of the tendon was fixed and the other end was placed as shown in Figure 11 and was attached to a single-dimensional tension sensor (DYLY-103, BIOFORCEN Co.). The tension sensor was connected to the stepper motor via a ball screw.

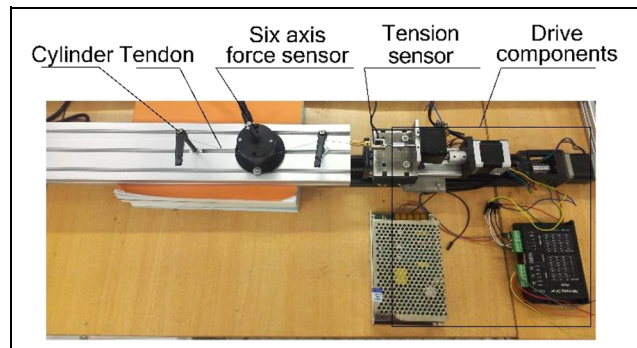


Figure 11. Three-point force measurement experiment.

After installation, the software was opened for the two sensors and run at the same time. The motor on the screw produced a slow linear motion that provided a small displacement. When the stepper motor moved slowly backward, the tension in the tendon increased as the range increased. The pressure P_r on the six-dimensional force sensor varied with changes in the tension F_r of the tendon. The tensile force F_r and the pressure P_r were uploaded to the host computer simultaneously. Ten representative datasets were selected (see Table 1) and were imported into MATLAB (MathWorks, <https://www.mathworks.com/>). A curve was then fitted using the least-squares method and the following formula for the tension was obtained:

Table 1. Data for calibration of sensors.

	1	2	3	4	5	6	7	8	9	10
Pressure P_r (N)	1.25	1.36	1.46	1.53	1.68	1.77	1.88	2	2.07	2.16
Tensile force F_r (N)	0.07	0.27	0.43	0.63	0.94	1.22	2.1	2.42	2.74	3.02

$$F_r = 3.437P_r - 4.514 \quad (37)$$

Under the preload of 1.1 N, the pressure required for a force of 1.63 N can be calculated using this formula.

Experiments on tendon-sheath transmission

Experimental design and devices

The tendon-sheath structure with the LeBus grooves system is controlled using an upper computer through a motion control card (GE-800-PG-PCI, Google Technology) that drives the stepper motor (model number 57H7630A4, Leadshine). The transmission error at the end of the system is measured using an incremental rotary encoder. The motor end is connected to the driving wheel, the follower wheel is connected to the load, and the driving wheel transmits the power from the follower wheel through the tendon-sheath system. All the transmission wheels and a variety of fixed brackets were constructed from nonmetallic materials that can be used in nuclear magnetic environments.

The sheath has a length of 1500 mm and the tests were conducted at cumulative bending angles of 180° and 540° with a friction coefficient of 0.16. The tendon was constructed using a polyethylene fiber with a diameter of 0.305 mm. The maximum tension value for the tendon was 20.8 kg, which was sufficient to satisfy the design requirements. The strength of the tendon was 2.8–4 N/tex, the modulus was 91–140 N/tex, and the density was 0.97–0.98 g/cm³. The tendon was wound on the new transmission wheel in two layers. The transmission wheel had a diameter of 25 mm.

First, the initial conditions were defined and the preload was set using the method described in the previous section. The same preload T_0 was applied to tendons 1 and 2 to ensure that the force on the input and output ends was balanced. The elongation of the tendons due to pre-tensioning forms part of the initial length.

Figure 12 shows a diagram of the experimental apparatus. Based on good pre-tightening of the tendon and using a motor speed of 0.05 m/s, the displacement transmission characteristics of the double-tendon-sheath system were tested and the results were compared with the theoretical data. The two-way displacement transmission of the system was compared with the experimental results for various values of the full curvature of the tendon and the load.

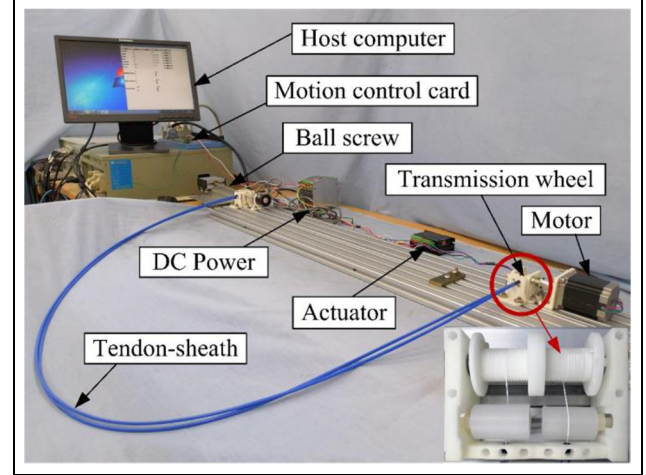


Figure 12. Experimental setup of tendon-sheath transmission system.

In the experiments, multiple datasets were tested for each experimental state. The average values of the multi-group data in the transmission were compared with the theoretical data values to calculate the error value of the system, as given by equation (38). In this study, the absolute value of the transmission deviation was recorded as the standard deviation.

$$\begin{aligned}
 e_{kj} &= s_{ij} - s_{oj} \quad j = 1, 2, 3, \dots, n, \\
 \bar{e}_j &= \frac{1}{n} \sum_{k=1}^n e_{kj} \quad k = 1, 2, 3, \dots, n, \\
 \sigma &= \sqrt{\frac{\sum_{k=1}^n (e_{kj} - \bar{e}_j)^2}{n-1}}
 \end{aligned} \quad (38)$$

where s_{ij} , s_{oj} , and e_{kj} denote the motor input displacement, the measured displacement of the encoder, and the deviation between these displacements at the j th moment of the k th group, respectively. \bar{e}_j is the mean value at the measurement point at the j th moment of the n th set of experimental data.

The experimental and theoretical results were compared and the average results from the multi-group experiments obtained under the two different conditions were analyzed. The positive trajectories are shown in Figure 13. The maximum positive error was 2.88 mm when the loading was 0.5 kg with a 180°

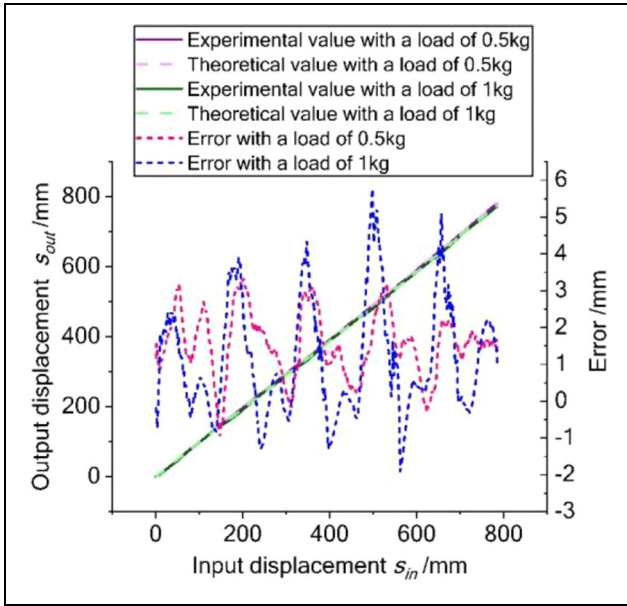


Figure 13. Comparison of positive trajectories from experiments and theory.

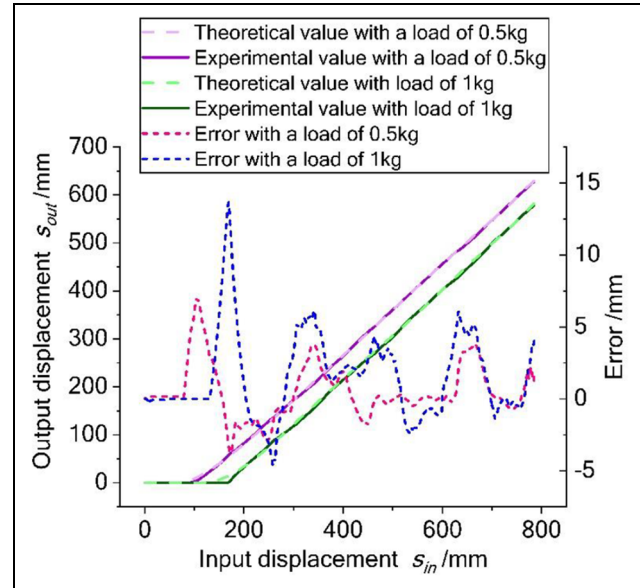


Figure 14. Comparison of negative trajectories from experiments and theory.

cumulative bending radius. The maximum positive error was 5.35 mm when the loading was 1 kg with a 540° cumulative bending radius. Furthermore, as shown in Figure 14, the maximum errors in the reverse hysteresis phase were 6.41 mm and 13.22 mm.

No significant differences were observed between the theoretical and experimental motion trajectories. The experimental trajectory was close to the theoretical trajectory, which thus verifies the correctness of the theoretical formulation.

Comparison of experimental data in three situations

Figure 15 shows the experimental data obtained from rotation of the driving wheels for one cycle when the tendon-sheath transmission system was loaded with 1 kg and 0.5 kg and when the cumulative bending radii were 180° and 540° . This figure represents a complete periodic displacement diagram for the positive and reverse motion of the double tendon-sheath system. The positive and negative signs represent the transmission directions. The transverse coordinate s_{in} is the displacement of the driving end, and the longitudinal coordinate s_{out} is the displacement of the follower end. $\dot{S}(+)$ and $\dot{S}(-)$ represent the speeds of the driving end and the follower end, respectively. The running direction (clockwise) at the beginning of the active end represents the positive direction. When the driving end was reversed, the elastic properties of the tendon material and the friction between the tendon and the sheath meant that the system at the follower end did not immediately produce any rotation in response to the

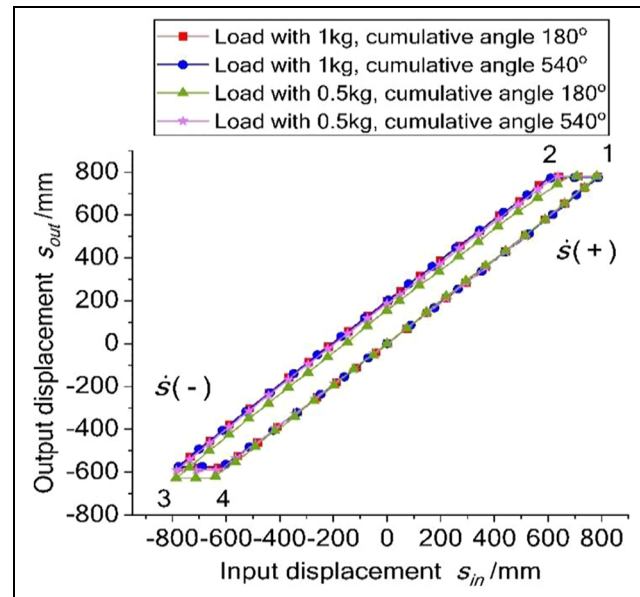


Figure 15. Displacement of the double tendon-sheath transmission system over one cycle.

movement of the driving end. The delay from the follower end is indicated by the movement from position 1 to position 2 in the figure. When the follower end overcomes the elastic relaxation and the friction, the follower wheel then begins to rotate. That is, the follower end moves after the driving end. Therefore, an apparent hysteresis phenomenon occurs when the tendon-sheath transmission system goes into reverse. When the hysteresis phenomenon ends, the motion is then transferred

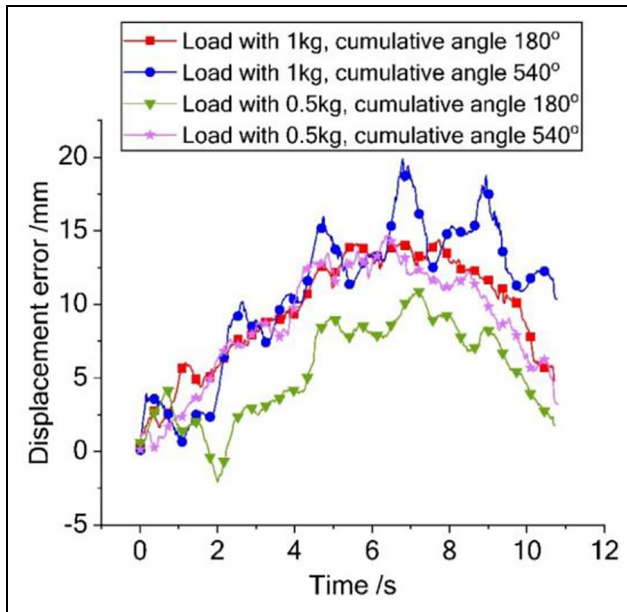


Figure 16. Displacement error of double tendon-sheath transmission system during positive movement.

smoothly. As shown by the straight line extending from position 2 to position 3, the movement from position 4 back to position 1 follows a similar curve in the counterclockwise direction.

Figure 16 shows the displacement error curves for the tendon-sheath system in the four cases after movement of 785 mm in the clockwise direction from the starting point. As shown in the graph, the displacement error with the larger cumulative bending radius was 10.37 mm under the 1 kg load, while the corresponding error with the smaller bending radius was 4.808 mm. The displacement error with the larger cumulative bending radius was 3.21 mm under the 0.5 kg load, while the corresponding error with the smaller bending radius was 1.77 mm. The experimental data indicate that the transmission error is generated from the transmission between the driving wheel and the follower wheel because of the characteristics of the tendon itself and the friction between the tendon and the sheath. Additionally, the displacement error will accumulate as the transmission distance increases. However, the displacement error increased gradually up to approximately 2/3 of the stroke, and the remaining 1/3 of the displacement error then decreased gradually. Because the majority of the tendon will be in the elastic elongation stage when the driving wheel rotates, the error will accumulate gradually. In the latter stages of the motion, the tensile force in the first half of the tendon will gradually increase with the winding of the driving wheel, thus resulting in greater tension than the initial tension at the driving end. Therefore, the rotational degree of the follower end will be greater than that of the driving

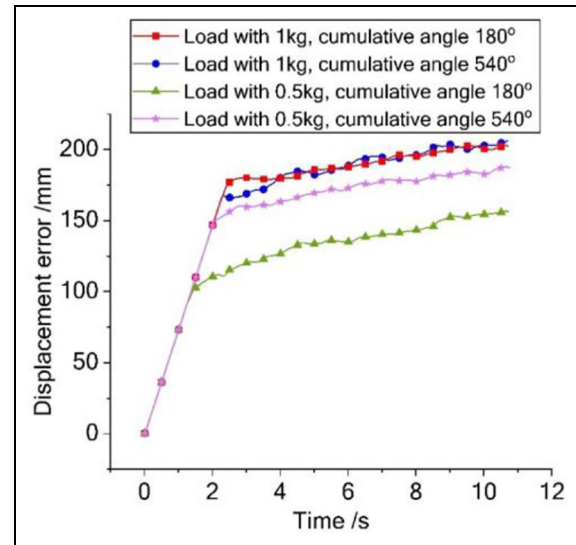


Figure 17. Displacement error of the double tendon-sheath transmission system during negative movement.

end in the later stages of the motion. The cumulative error is thus lower during the early stages.

Figure 17 shows the displacement error of the reverse movement that followed the positive movement of the double tendon-sheath system. The displacement error with the larger bending radius was 205.99 mm under the load of 1 kg during reverse operation, while that with the smaller bending radius was 202.33 mm. Under the 0.5 kg load, the displacement error with the larger bending radius was 187.06 mm, while that with the smaller bending radius was 156.28 mm. During the initial stages of the transmission, the tendon gradually changes from the relaxation stage to the tensioning stage. Therefore, the follower wheel does not immediately produce any movement in tandem with the rotation of the driving end. When the driving end overcomes the relaxation of the tendon and gradually becomes tensioned, the follower wheel then begins to move. Because of the coupling characteristics of the double tendon-sheath system, the error after the change in direction was much greater than that observed during positive driving.

Figure 17 also shows that a larger cumulative bending radius will produce more friction in both the transmission and the reverse hysteresis, regardless of the transmission load. These experimental data indicate that when the same cumulative bending radius is used, a greater positive error increment is observed in the system with the heavier load. The hysteresis increment in the system with the heavier load was smaller than that in the system with the smaller load after the change in the transmission direction. Because the cumulative bending radius increased, the friction force of the tendon also increased. However, the increase in the load

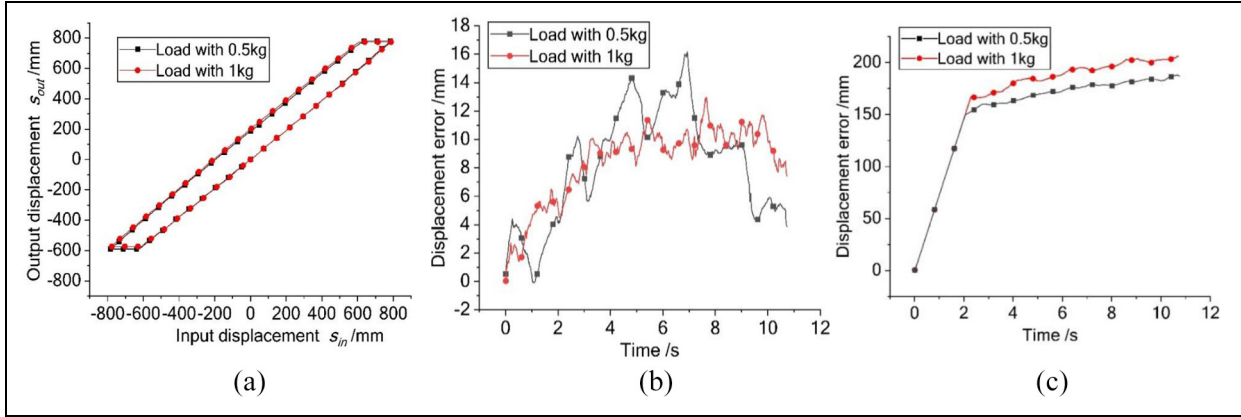


Figure 18. Comparison between different loads at the same cumulative bending radius.

meant that the larger cumulative radius produced more friction, which then led to a higher positive transmission error. The relaxation increment in the tendon under a larger load would be smaller than the increment under a lighter load. Therefore, when the cumulative bending radius increased, the increment in the hysteresis for the transmission system with the larger load was less than that for the transmission system with the smaller load. Similar conclusions to those of the previous theories could be determined based on the characteristics of the theoretical formula.

Figure 18 compares the experimental data acquired under different transmission system loads for the same cumulative bending angle. The positive movement of the driving wheel was 785 mm, and the displacement errors under loads of 0.5 kg and 1 kg were 3.85958 mm and 7.42479 mm, respectively. For the reverse operation, the displacement errors under loads of 0.5 kg and 1 kg were 187.09167 mm and 205.99708 mm, respectively. The figure shows that when the cumulative bending radius is the same, a heavier load results in greater positive and reverse errors. The larger load means that greater tension is required and this results in greater friction.

Compensation experiments

The proposed tendon-sheath system is driven using a stepper motor. The elastic tension and the bending of the sheath, along with the friction between the tendon and the sheath and that between the tendon and the transmission wheel, will lead to some errors during movement. By establishing appropriate formulas for the transmission characteristics of the tendon-sheath system, the forward and reverse errors can then be calculated using the driving input force at the proximal end. However, the large-scale transfer characteristics of the system described in this paper cannot be compensated by simply measuring the proximal force. The

particular nature of the application environment means that encoders that are suitable for nuclear magnetism applications must be used.

By measuring the displacement of the follower end during the initial stage of the movement, the initial pull power could be calculated in real time, and the corresponding tendon elongation and system hysteresis characteristics could then be estimated by calculating the initial tensile force. In this way, the system could be fed forward, thus compensating for both the positive displacement transmission and the hysteresis characteristics of the reverse motion. In addition, the compensation reflection time of the system could be reduced. Using the data collected by the encoder, error compensation could also be performed in real time. Therefore, the corresponding transmission error model can be expressed as follows:

$$\begin{aligned}\theta_{ain} &= \theta_{aw}^+ + \theta_{out}^+ \\ \theta_{bin} &= \theta_{bw}^- + \theta_{out}^- + \theta_b\end{aligned}\quad (39)$$

where $\theta_{aw}^+ = \Delta L_{aw}^+ / r$, and $\theta_{bw}^- = \Delta L_{bw}^- / r$.

The proposed system is designed such that the tendon is subjected to multi-layer winding in both the driving wheel and the follower wheel. The nonlinearity of the tendon material produces viscous friction, and the tendon and sheath motions during transmission also generate friction. Therefore, the LuGre friction model²⁸ was used to compensate for the nonlinear sliding deformation and friction hysteresis during the transmission process.

The mathematical expressions for the LuGre friction model are given as follows:

$$\begin{cases} f = \sigma_0 z + \sigma_1 \dot{z} + \sigma_2 \dot{x} \\ \dot{z} = \dot{x} - \frac{|\dot{x}|}{g(\dot{x})} z \\ g(\dot{x}) = f_c + (f_s - f_c) \exp[-(x/v_s)^2] \end{cases}\quad (40)$$

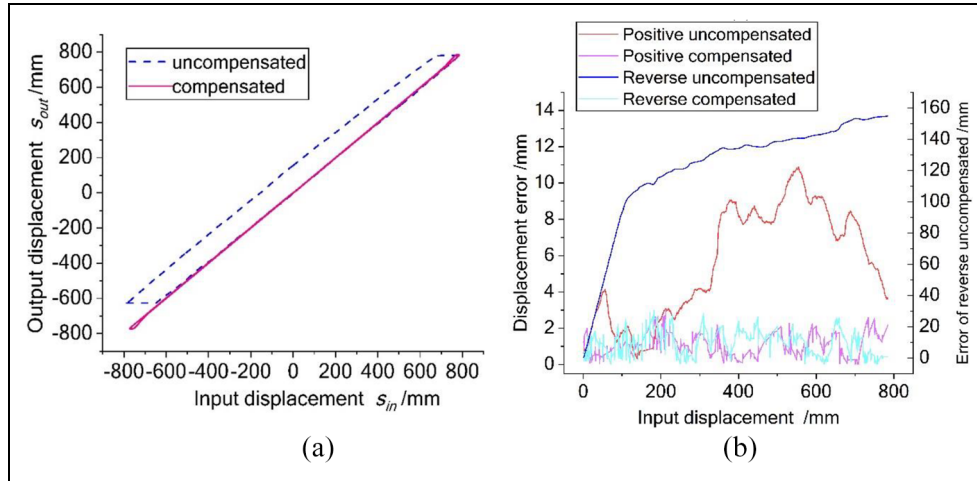


Figure 19. Comparison of experimental motion trajectories and errors before and after compensation under a load of 0.5 kg with a cumulative angle of 180° .

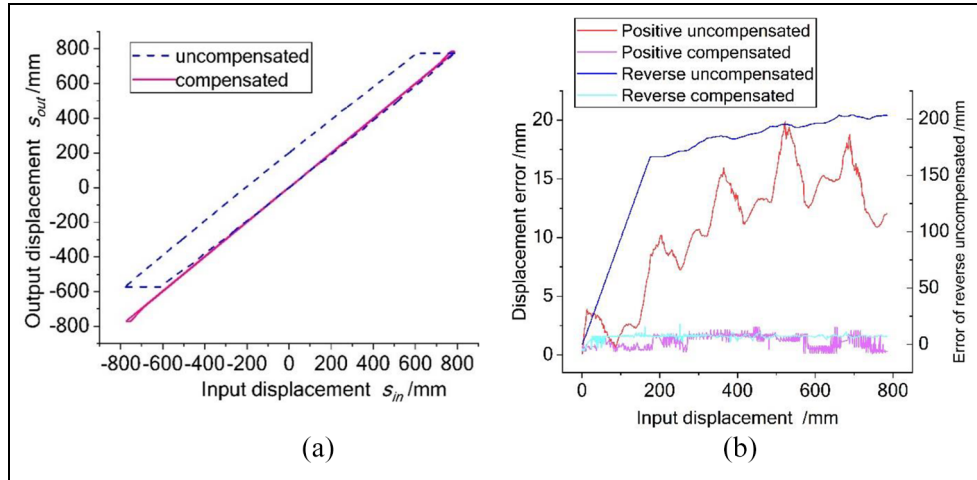


Figure 20. Comparison of experimental motion trajectories and errors before and after compensation under a load of 1 kg with a cumulative angle of 540° .

where the coefficients σ_0 , σ_1 , and σ_2 are the stiffness coefficient, the micro-damping coefficient and the viscous friction coefficient of the system, respectively. z is the average deformation of the contact surface bristles and \dot{x} is the relative velocity of the motion between the two contact surfaces. The Stribeck phenomenon is described using $g(\dot{x})$, which is a function of a constant greater than zero. f is the friction, f_c is the Coulomb friction, f_s is the static friction, and v_s is the Stribeck speed of the system.

The parameters of the LuGre model can be identified from the experimental data using the least-squares method and a genetic algorithm. In this study, we found that the static friction factor $\mu_s = 0.16$, the bristle stiffness $k = 1 \times 10^5/(N/m)$, the microscopic damping coefficient $\sigma_1 = 1 \times 10^{2.5}/(N \bullet s/mm)$, the viscous friction

coefficient $\sigma_2 = 4.3$, and the Stribeck speed $v_s = 1 \times 10^{-5}(m/s)$. A compensation program was written into the control program of the Googol motion control card in the host computer using the C++ language. The following two cases were then compensated: the load of 0.5 kg with a cumulative angle of 180° and the load of 1 kg with a cumulative angle of 540° . The results are shown in Figures 19 and 20, respectively.

Figures 19(a) and 20(a) show the experimental motion trajectories. A significant error was still present in the commutative hysteresis phase when no compensation control was applied. However, the hysteresis error of the positive motion was reduced significantly after the compensation. Although the compensation can reduce the hysteresis error, the actual relationship between the input and the output remains nonlinear.

Figures 19(b) and 20(b) show the average and standard deviations of the errors of the double tendon-sheath system in the positive and hysteresis stages for the two experimental cases. Using the compensation mechanism, the positive operating error could be controlled in the range from 1.14–1.24 mm and the average hysteresis error could be controlled in the range from 1.32–1.59 mm. These results are sufficient to meet the requirements of long-distance and large-stroke transmission applications.

Conclusions

In this article, based on the critical driving technology requirements for robots operating in nuclear magnetic environments, a new type of double tendon-sheath transmission system has been proposed that offers long-distance and large-stroke power transmission. The proposed system uses a double broken-line groove structure that can effectively avoid the phenomenon of tendon entanglement when the tendon is wound. Therefore, the transmission accuracy can be improved further. The friction model of the tendon winding process and the transmission and hysteresis model of the tendon-sheath system have been established, and an experimental device was constructed. The experimental data were compared with the theoretical model to verify the correctness of the model.

Experiments were conducted under various conditions and the special transmission law of tendon-sheath transmission was derived. On this basis, the friction and hysteresis phenomena were compensated and precise position control was realized. A position compensation experiment demonstrated the validity of the proposed compensation mechanism and the improved control performance. The tendon-sheath transmission system proposed in this article is not limited to application to robots for use under nuclear magnetism conditions. The proposed system could be used for any robot that requires long-distance, large-stroke transmission, and the paper provides a theoretical basis for researchers who wish to achieve this functionality.

The goal for future work on this system is integration of this unique tendon-sheath system and breast intervention robots into medical experiments. In this study, the experimental platform was only applied to degree of freedom (DOF) control of the robot joints. Therefore, to meet the requirements of these robot applications, multiple-DOF (more than five) movements that combine advanced robotic technology with measurement technology will be studied. Furthermore, a rigid–flexible coupling analysis between the robot end and human tissues will be investigated to enable more complex tasks (e.g., removing target tissue while bypassing blood vessels) to be performed. In addition,

tactile problems must also be considered to help surgeons to perceive organizational stress.


Declaration of conflicting interests

The author(s) declared no potential conflicts of interest with respect to the research, authorship, and/or publication of this article.

Funding

The author(s) disclosed receipt of the following financial support for the research, authorship, and/or publication of this article: The work was supported by the National Natural Science Foundation of China (51675142) and the Natural Science Foundation of Heilongjiang Province (ZD2018013).

ORCID iD

Yongde Zhang  <https://orcid.org/0000-0003-4602-1563>

References

1. Bray F, Ferlay J, Soerjomataram I, et al. Global cancer statistics 2018: GLOBOCAN estimates of incidence and mortality worldwide for 36 cancers in 185 countries. *CA Cancer J Clin* 2018. DOI: 10.3322/caac.21492.
2. Christopherson KM and Smith BD. How does MR imaging help care for my breast cancer patient? Perspective of a radiation oncologist. *Magn Reson Imaging Clin N Am* 2018; 26: 295–302. DOI: 10.1016/j.mric.2017.12.007.
3. Zhang Y, Jia X, Jiang J, et al. Recent advances on breast intervention surgery robot. *Recent Patents on Engineering* 2016; 10: 187–195.
4. Monfaredi R, Cleary K and Sharma K. MRI robots for needle-based interventions: Systems and technology. *Ann Biomed Eng* 2018; 46: 1479–1497. DOI: 10.1007/s10439-018-2075-x.
5. Stoianovici D, Jun C, Lim S, et al. Multi-imager compatible, MR safe, remote center of motion needle-guide robot. *IEEE Trans Biomed Eng* 2018; 65: 165–177. DOI: 10.1109/TBME.2017.2697766.
6. Zhang Y, Shi C, Du H, et al. A MRI compatible robot for breast intervention. In: *2015 IEEE International Conference on Robotics and Biomimetics (ROBIO)*, 2015, pp. 2472–2477. IEEE.
7. Su H, Li G and Fischer GS. *Sensors, actuators, and robots for MRI-guided surgery and interventions. Volume 3: Image-guided surgical procedures and interventions*. 2018, pp. 201–231. DOI: 10.1142/9789813232303_0008.
8. Chen Y, Godage I, Su H, et al. Stereotactic systems for MRI-guided neurosurgeries: A state-of-the-art review. *Ann Biomed Eng* 2019; 47: 335–353. DOI: 10.1007/s10439-018-02158-0.
9. Su H, Li J, Kong K, et al. Development and experiment of the Internet-based telesurgery with MicroHand robot. *Advances in Mechanical Engineering* 2018; 10. DOI: 10.1177/1687814018761921.
10. Troccaz J, Dagnino G and Yang GZ. Frontiers of medical robotics: From concept to systems to clinical translation. In: Yamush ML (ed) *Annual Review of Biomedical*

- Engineering, Vol 21*. Palo Alto: Annual Reviews, 2019, pp. 193–218.
11. Kim YJ. Anthropomorphic low-inertia high-stiffness manipulator for high-speed safe interaction. *IEEE Trans Robot* 2017; 33: 1358–1374. DOI: 10.1109/tro.2017.2732354.
 12. Wang K-Y, Yin P-C, Yang H-P, et al. The man-machine motion planning of rigid-flexible hybrid lower limb rehabilitation robot. *Advances in Mechanical Engineering* 2018; 10. DOI: 10.1177/1687814018775865.
 13. Aktan ME and Akdoğan E. Design and control of a diagnosis and treatment aimed robotic platform for wrist and forearm rehabilitation: DIAGNOBOT. *Advances in Mechanical Engineering* 2018; 10. DOI: 10.1177/1687814017749705.
 14. Kaneko M, Paetsch W and Tolle H. Input-dependent stability of joint torque control of tendon-driven robot hands. *IEEE Trans Ind Electron* 1992; 39: 96–104.
 15. Kaneko M, Yamashita T and Tanie K. Basic considerations on transmission characteristics for tendon drive robots. In: *Fifth International Conference on Advanced Robotics (91 ICAR), 'Robots in Unstructured Environments'*, 1991, pp. 827–832. IEEE.
 16. Palli G, Borghesan G and Melchiorri C. Modeling, identification, and control of tendon-based actuation systems. *IEEE Trans Robot* 2012; 28: 277–290.
 17. Agrawal V, Yao B and Peine WJ. Modeling of viscoelastic cable-conduit actuation for MRI compatible systems. *J Dyn Sys Meas Control* 2013; 135: 051004.
 18. Agrawal V, Peine WJ and Yao B. Modeling of transmission characteristics across a cable-conduit system. *IEEE Trans Robot* 2010; 26: 914–924. DOI: 10.1109/tro.2010.2064014.
 19. Le HM, Do TN and Phee SJ. A survey on actuators-driven surgical robots. *Sens Actuator A Phys* 2016; 247: 323–354. DOI: 10.1016/j.sna.2016.06.010.
 20. Nguyen TL, Allen SJ and Phee SJ. Direct torque control for cable conduit mechanisms for the robotic foot for footwear testing. *Mechatronics* 2018; 51: 137–149. DOI: 10.1016/j.mechatronics.2018.03.004.
 21. Do TN, Tjahjowidodo T, Lau MWS, et al. Adaptive control for enhancing tracking performances of flexible tendon–sheath mechanism in natural orifice transluminal endoscopic surgery (NOTES). *Mechatronics* 2015; 28: 67–78. DOI: 10.1016/j.mechatronics.2015.04.002.
 22. Letier P, Schiele A, Avraam M, et al. Bowden cable actuator for torque-feedback in haptic applications. In: *Proc Eurohaptics 2006 Conf*, 2006.
 23. Schiele A, Letier P, Van Der Linde R, et al. Bowden cable actuator for force-feedback exoskeletons. In: *2006 IEEE/RSJ International Conference on Intelligent Robots and Systems*, 2006, pp. 3599–3604. IEEE.
 24. Yang Y, Jiang S, Yang Z, et al. Design and analysis of a tendon-based computed tomography-compatible robot with remote center of motion for lung biopsy. *Proc Inst Mech Eng H* 2017; 231: 286–298. DOI: 10.1177/0954411917690763.
 25. Jiang S, Lou J, Yang Z, et al. Design, analysis and control of a novel tendon-driven magnetic resonance-guided robotic system for minimally invasive breast surgery. *Proc Inst Mech Eng H* 2015; 229: 652–669. DOI: 10.1177/0954411915599018.
 26. Zhang Q, Wang X, Tian M, et al. Modeling of novel compound tendon-sheath artificial muscle inspired by Hill muscle model. *IEEE Trans Ind Electron* 2018; 65: 6372–6381. DOI: 10.1109/tie.2017.2784377.
 27. Wu Q, Wang X, Chen L, et al. Transmission model and compensation control of double-tendon-sheath actuation system. *IEEE Trans Ind Electron* 2015; 62: 1599–1609. DOI: 10.1109/tie.2014.2360062.
 28. Piatkowski T. Dahl and LuGre dynamic friction models—The analysis of selected properties. *Mech Mach Theory* 2014; 73: 91–100.